Macromolecules

Article

pubs.acs.org/Macromolecules

Asymmetric Giant "Bolaform-like" Surfactants: Precise Synthesis, Phase Diagram, and Crystallization-Induced Phase Separation

Kan Wu,[†] Mingjun Huang,[†] Kan Yue,*[,†] Chang Liu,[†] Zhiwei Lin,[†] Hao Liu,[†] Wei Zhang,[†] Chih-Hao Hsu,[†] An-Chang Shi,[‡] Wen-Bin Zhang,*[,§] and Stephen Z. D. Cheng*[,†]

[†]Department of Polymer Science, College of Polymer Science and Polymer Engineering, The University of Akron, Akron, Ohio 44325-3909, United States

[‡]Department of Physics and Astronomy, McMaster University, Hamilton, Ontario, Canada L8S 4M1

[§]Key Laboratory of Polymer Chemistry & Physics of Ministry of Education, Center for Soft Matter Science and Engineering, College of Chemistry and Molecular Engineering, Peking University, Beijing 100871, P. R. China

Supporting Information

ABSTRACT: A series of unique heterofunctionalized asymmetric giant "bolaform-like" surfactants composed of a polystyrene (PS) chain end-capped with two distinctly functionalized polyhedral oligomeric silsesquioxane (POSS) cages [one with seven isobutyl groups (BPOSS) and the other with 14 hydroxyl groups (DPOSS)] were designed and synthesized, and their self-assembly behaviors were investigated. Combining the atomic transfer radical polymerization using a BPOSS-containing initiator and the sequential "click" approach, BPOSS-PS$_n$-DPOSS samples with different PS molecular weights were obtained. Investigation on their self-assembly behaviors revealed that they could form a variety of different ordered structures, such as lamellae, double gyroids, hexagonally packed cylinders, and body-center-cubic spheres, with feature sizes around or below 10 nm. Functional groups on the POSS cages govern the interaction parameters of different POSS cages with the PS interconnect and thus their compatibility. Hydrophilic DPOSS cages are phase-separated from the PS domains, while BPOSS cages are favorably associated within the PS domains. However, in the lamellae phase where the geometry of confinement seems compatible with the close-packing of BPOSS, the BPOSS cages tend to crystallize due to the existence of the flat interfaces, leading to further phase separation of the BPOSS cages from the PS interconnects. These results provide insights into the design of novel self-assembling materials based on POSS−polymer conjugates toward desired physical properties.

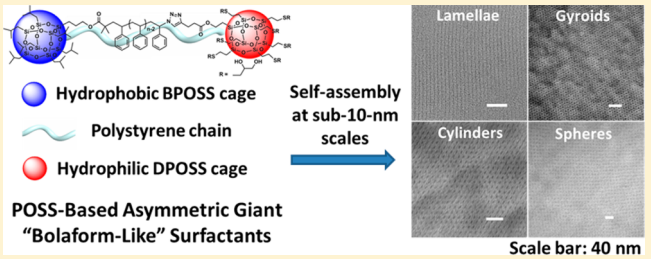

INTRODUCTION

The study of self-assembling[1,2] materials has been one of the most important themes in materials research during the past decades due partly to their potential applications in the "bottom-up" fabrication of complicated nanostructures and nano-objects beyond the reach of traditional top-down lithographic techniques.[3,4] To this end, block copolymers, consisted of chemically connected polymeric blocks of different compositions, are of particular interests because of their intriguing self-assembly behaviors under different processing conditions and environments,[5,6] indicating widespread potentials in various technological applications. In the bulk state, driven by the chemical incompatibility of the compositionally different blocks, a variety of self-assembled ordered structures are generated.[6,7] Take the simplest diblock copolymers as an example, both theoretical calculations[8,9] and experimental observations[10−12] reveal the formation of different nanophase-separated structures depending on the volume fraction of individual blocks, among which lamellae (Lam), double gyroids (DG), hexagonally packed cylinders (Hex), and body-centered cubic spheres (BCC) represent the most common cases.[7] Nanophase separation takes place when the segregation strength characterized by the parameter χN, where χ is the Flory−Huggins parameter between the two blocks and N is total degree of polymerization of the block copolymer, exceeds a critical value (typically ∼10.5) based on the mean-field theory.[7]

One unique advantage related to the nanophase separation phenomena is the ability to generate ordered patterns at sub-20 nm length scales via a bottom-up approach.[3,13] However, to further decrease the sizes of the nanophase-separated domains, the degree of polymerization of each segment should be lowered. The resulting lower χN values, in many diblock copolymer systems, fail to provide the thermodynamic driving force toward strong phase separation. One practical solution to tackle this problem is to develop high-χ block copolymers, such as silicon-containing[14−16] and metal-containing[17,18] block

Received: May 15, 2014
Revised: June 25, 2014

   dx.doi.org/10.1021/ma501017e | Macromolecules XXXX, XXX, XXX−XXX

copolymers, among others. Many recent reports have shown phase separated domains below 10 nm in thin films.[14,15,19,20]

An alternative strategy is to design other nanoscale building blocks to replace one of the polymer blocks, resulting in novel hybrid polymers.[21−23] Advantages of this strategy are that incorporating nonpolymeric building blocks may provide sufficiently high interaction parameter to induce nanophase separation with smaller macromolecular blocks, thus generating phase-separated domains with feature sizes below 10 nm. Additionally, if a building block with a precise primary chemical structure is used as one segment in these hybrid polymers, the molecular weight heterogeneity of the conjugates is only from the polymer chain, and thus, uniform nanopatterns can be potentially generated. Recent examples include the use of oligosaccharide species to construct hybrid block copolymers for self-assembled structures with sub-10 nm feature sizes.[21−23]

In our group, we have been devoted to use molecular nanoparticles (MNPs), such as functionalized [60]-fullerene[24−27] and polyhedral oligomeric silsesquioxane (POSS)[28−31] derivatives, as the essential building blocks in the design and synthesis of novel hybrid polymers. Regular POSS molecules are a family of cage-like structures with silicon−oxygen backbones.[30,31] Their precisely defined structures, shape rigidity, and tunable periphery groups make them ideal building blocks for the construction of various hybrid materials, especially in the field of macromolecular science.[32−35] Studies on POSS-containing polymers can be traced back to about two decades ago, mainly focusing on how the chemically attached POSS cages affect the mechanical and thermal properties of the hybrid polymers.[34,36] Recently, Hayakawa et al. reported synthesis and self-assembly of POSS-containing block copolymers, where alkyl-substituted POSS cages are chemically attached to each repeating unit of one polymer block.[37−39] Nanophase-separated structures between the polystyrene (PS) blocks and the POSS-containing blocks are demonstrated, and the inter-row spacing of the POSS-containing cylinders can reach 12 nm in directed self-assembled Hex phase in the thin film state.[39]

We envision that one single properly functionalized POSS cage can replace a polymeric block in constructing block copolymers. For instance, the simplest POSS−polymer architecture composed of one POSS cage tethered with one polymer tail can be viewed as an analogue of a diblock copolymer. It could also be viewed as the size-amplified version of small-molecule surfactants and thus are also referred to as giant surfactants.[40−43] We have demonstrated that giant surfactants based on MNPs (such as POSS and fullerene derivatives) and polymers (such as PS) can indeed self-assemble into various well-ordered nanostructures, and their self-assembled structures possess remarkable sensitivity on molecular architectures in the bulk, thin film, and solution states.[41,42] The rich structure variations of POSS−polymer conjugates are thus of great interest and worthy of further investigations to fully reveal the structure−property relationship of these nanomaterials.

To further advance our study of this class of POSS-based hybrid polymer materials, it is desirable to extend our molecular designs to achieve more compositional and architectural variations. We have reported the preparations of POSS-based giant surfactants with increasing molecular complexity,[43−48] for example, one POSS head tethered with different polymer tails,[43] cyclic PS tethered with one POSS head,[48] and others. On the other hand, since the properties of POSS cages can be tuned by changing their periphery functional groups, introducing two different functionalized POSS cages onto the both ends of one polymer chain as an interconnect could possibly create molecular architectures similar to triblock copolymers. Isobutyl-substituted POSS (BPOSS) derivatives are commercially available and known to be crystalline (favorably interacting with each other);[37,38] it is interesting to study how the self-assembly behaviors are affected by incorporating both of a crystalline hydrophobic BPOSS and an amorphous hydrophilic POSS (e.g., DPOSS) onto a polymer interconnect.

In this article, we report the molecular design, synthesis, and self-assembly in the bulk state of a set of novel POSS-based giant "bolaform-like" surfactants (BPOSS-PS$_n$-DPOSS). Usually, bolaform surfactant refers to those with two polar head groups interconnected by a nonpolar hydrophobic chain.[49] In our case, we designed and synthesized a slightly different one: a hydrophobic polystyrene chain interconnected by one amorphous polar head and one crystalline nonpolar head. Therefore, we call it giant "bolaform-like" surfactant. The structural uniqueness is reflected by the chemical attachments of two distinct POSS cages with different periphery functional groups at both ends of a PS chain. Synthesis of this novel structure is accomplished in a highly efficient manner, combining the controlled atomic transfer radical polymerization (ATRP) and the reported sequential "click" approach.[44,45,48,50] The current study provides the first design of an asymmetric giant "bolaform-like" surfactant composed of two distinctly functionalized MNPs interconnected with a polymer chain. It is intriguing to study how the self-assembly behaviors are influenced by periphery chemical functional groups of the POSS derivatives, providing insights into further guiding the designs and syntheses of POSS−polymer giant surfactants.

EXPERIMENTAL SECTION

Chemicals and Solvents. Toluene (EMD, ACS grade) and styrene (99%, Sigma-Aldrich) were purified as previously reported.[51] Methanol (Fisher Scientific, reagent grade), chloroform (Fisher Scientific, Certified ACS), dichloromethane (DCM, Fisher Scientific), ethyl acetate (Fisher Scientific), tetrahydrofuran (THF, Fisher Scientific), *N*,*N*-dimethylformamide (DMF, anhydrous 99.8%, Sigma-Aldrich), and hexanes (Fisher Scientific, Certified ACS) were used as received. 4-Pentynoic acid (98%, Acros Organics), *N*,*N*′-diisopropylcarbodiimide (DIPC, 99%, Acros Organics), 4-dimethylaminopyridine (DMAP, ≥99%, Sigma-Aldrich), copper(I) bromide (98%, Acros Organics), *N*,*N*,*N*′,*N*″,*N*″-pentamethyldiethylenetriamine (PMDETA, 99%, Sigma-Aldrich), 1-thioglycerol (≥98%, Fluka), ethyl 2-bromo-2-methylpropionate (98%, Sigma-Aldrich), sodium azide (ReagentPlus, ≥99.5%, Sigma-Aldrich), α-bromoisobutyryl bromide (BIBB, 98%, Sigma-Aldrich), *N*,*N*-diisopropylethylamine (DIPEA, ≥99%, Sigma-Aldrich), 2-hydroxy-4′-(2-hydroxyethoxy)-2-methylpropiophenone (Irgacure 2959, 98%, Sigma-Aldrich), PSS-(3-hydroxypropyl)-heptaisobutyl-substituted (BPOSS-OH, Sigma-Aldrich), and OctaVinyl-POSS (>97%, Hybrid Plastics) were used as received. VPOSS-alkyne was synthesized as previously described.[50]

Characterizations. *Nuclear Magnetic Resonance (NMR) Spectroscopy.* All ^{1}H, ^{13}C, and ^{29}Si NMR spectra were obtained in $CDCl_3$ (Sigma-Aldrich, 99.8% D) as solvent using a Varian NMRS 500 spectrometer except where stated elsewhere. Tetramethylsilane was used as the internal standard whenever necessary. The resonance frequencies for ^{1}H, ^{13}C, and ^{29}Si nuclei are 500, 125, and 100 MHz, respectively. The ^{1}H NMR spectra were referenced to the residual proton impurities in $CDCl_3$ at δ 7.27 ppm, the ^{13}C NMR spectra were referenced to $^{13}CDCl_3$ at δ 77.00 ppm, and the ^{29}Si NMR spectra were referenced to tetramethylsilane in the $CDCl_3$ at δ 0.00 ppm.

dx.doi.org/10.1021/ma501017e | *Macromolecules* XXXX, XXX, XXX−XXX

Fourier-Transform Infrared (FTIR) Spectroscopy. Infrared spectra of the polymer products were recorded on an Excalibur Series FT-IR spectrometer (DIGILAB, Randolph, MA) by casting polymer films on KBr plates from polymer solutions in THF with subsequent drying at room temperature by blowing air. The data were processed using the Win-IR software.

Size Exclusion Chromatography (SEC). SEC analyses for the synthesized hybrid polymers were performed on a Waters 150-C Plus instrument equipped with three HR-Styragel columns [100 Å, mixed bed (50/500/10^3/10^4 Å), mixed bed (10^3, 10^4, 10^6 Å)], and a triple detector system. The three detectors included a differential viscometer (Viscotek 100), a laser light scattering detector (Wyatt Technology, DAWN EOS, λ = 670 nm), and a differential refractometer (Waters 410). THF was used as the eluent with a flow rate of 1.0 mL/min at room temperature. Data processing was accomplished using the software on a workstation equipped with this system.

Matrix-Assisted Laser Desorption/Ionization Time-of-Flight (MALDI-TOF) Mass Spectroscopy. MALDI-TOF mass spectra of the hybrid samples were recorded on a Bruker Ultraflex III TOF/TOF mass spectrometer (Bruker Daltonics, Billerica, MA), equipped with a Nd:YAG laser which emits at a wavelength of 355 nm. The matrix compound used was *trans*-2-[3-(4-*tert*-butylphenyl)-2-methyl-2-propenylidene]malononitrile (DCTB, >99%, Aldrich) and was dissolved in $CHCl_3$ at a concentration of 20.0 mg/mL. Sodium trifluoroacetate (NaTFA) was used as the cationizing agent and was prepared as the MeOH/$CHCl_3$ (v/v = 1/3) solution at a concentration of 10.0 mg/mL. The matrix and cationizing agent solutions were mixed in the ratio of 10/1 (v/v). The sample was prepared by depositing 0.5 μL of matrix and salt mixture on the wells of a 384-well ground-steel plate, allowing the spots to dry, depositing 0.5 μL of each sample on a spot of dry matrix, and adding another 0.5 μL of matrix and salt mixture on top of the dry sample (the sandwich method).[52] Mass spectra were measured in the reflection mode, and the mass scale was calibrated externally with a polystyrene or PMMA standard at the molecular weight region under consideration. Data analyses were conducted with Bruker's flexAnalysis software.

Transmission Electron Microscopy (TEM). A JEOL-1230 transmission electron microscope (TEM) with an accelerating voltage of 120 kV was utilized to record the bright field images of the hybrid polymers. TEM images were taken on a digital CCD camera and processed with the accessory digital imaging system.

Thermogravimetric Analysis (TGA). The nonisothermal decomposition experiments were carried out in a thermogravimetric analysis instrument (Model Q500, TA Instruments) under a nitrogen atmosphere for the temperature range of 30−650 °C with a heating rate of 10 °C/min. Initial mass of the sample was ca. 5 mg for each run of the experiments. A platinum crucible was used as the sample holder.

Differential Scanning Calorimetry (DSC). Thermal properties were characterized utilizing a PerkinElmer PYRIS Diamond DSC with an Intracooler 2P apparatus. The temperature and heat flow scales were calibrated at different heating and cooling rates (1−40 °C/min) using a series of standard materials.

Small-Angle X-ray Scattering (SAXS). SAXS experiments were performed on a Rigaku MicroMax 002+ instrument equipped with a two-dimensional (2D) multiwire area detector and a microfocus sealed copper tube. The working voltage and current for the X-ray tube are 45 kV and 0.88 mA, respectively. The wavelength of the X-ray is 0.154 nm. The scattering vector (q) was calibrated using silver behenate with the primary reflection peak at (q = 1.067 nm^{-1}). The SAXS diffraction patterns covering the q value range between 0.3 and 2.9 nm^{-1} were recorded. The recording time for each data was 5−10 min, depending on the scattering intensity. The data were analyzed with SAXSgui software.

Wide-Angle X-ray Diffraction (WAXD). WAXD experiments were conducted on the instrument equipped with a Rigaku 18 kW rotating anode generator and an image plate as the detector. The instrument was calibrated using silicon powders with 2θ being 28.4° under Cu Kα radiation in the high angle region and silver behenate in the low angle region. The air scattering was subtracted. The 1D WAXD curve was integrated from the 2D image.

Sample Preparations for SAXS Measurements and Microtomed Samples for TEM Experiments. The vacuum-dried powder hybrid polymers were put into an aluminum sample holder with a hole of 5 mm diameter and sealed with Kapton tapes. The holder was heated to 150 °C under nitrogen atmosphere and annealed at that temperature for 30 min to several hours depending on the sample conditions. After the thermal annealing, these samples were used in SAXS measurements. Thin slices of the bulk samples were obtained using a Reichert Ultracut S (Leica) microtome on annealed samples embedded in epoxy monolith at room temperature. The slices were transferred to copper grids coated with amorphous carbon for TEM experiments. The thickness of these slices was around 70−100 nm. When necessary, staining of the samples was performed using osmium tetroxide for 12 h at room temperature.

Calculations of Molecular Parameters for BPOSS-PS$_n$-DPOSS Samples. Molecular weights of the samples were obtained from NMR measurements based on the ratio between the peak area integrations in the ^{1}H NMR spectra at δ 7.40−6.32 ppm (aromatic protons in PS) and the characteristic methyl peaks on the BPOSS cage (42H at ca. δ 1.02 ppm for one BPOSS cage). The peak area of the $CHCl_3$ residue was estimated using the tetramethylsilane internal standard. This ratio gives the number-average degree of polymerization, n, of the PS polymeric block for each sample. Molecular weights of the BPOSS-PS$_n$-XPOSS samples can be obtained by the summation of $M_{n,PS}$ (n × 104.1 Da), $M_{Initiator}$ (1022.2 Da), and M_{XPOSS} (773.2 Da for VPOSS and 1530.3 Da for DPOSS, including the linker between BPOSS/DPOSS and PS).

Calculations of the volume fractions of the BPOSS, PS, and DPOSS domains were based on the reported density data of the three blocks. It is assumed that the density of pure POSS cages with the same functional groups is identical to that of the POSS cage in the self-assembled structures of the hybrid polymers. The density values are 1.13 g/cm^3 for the BPOSS cage,[53] 1.43 g/cm^3 for the DPOSS cage,[41] and 1.05 g/cm^3 for PS. The volume fraction of PS is given by eq 1

$$f_{PS} = \frac{M_{PS}/\rho_{PS}}{M_{PS}/\rho_{PS} + M_{BPOSS}/\rho_{BPOSS} + M_{DPOSS}/\rho_{DPOSS}} \quad (1)$$

where the molecular weight of the DPOSS building block M_{DPOSS} = 1.5 kg/mol, the molecular weight of the BPOSS building block M_{BPOSS} = 1.0 kg/mol, and M_{PS} is the molecular weight of PS determined from NMR data. Similarly, the volume fraction of BPOSS is given by eq 2

$$f_{BPOSS} = \frac{M_{BPOSS}/\rho_{BPOSS}}{M_{PS}/\rho_{PS} + M_{BPOSS}/\rho_{BPOSS} + M_{DPOSS}/\rho_{DPOSS}} \quad (2)$$

and the volume fraction of DPOSS can be estimated by eq 3

$$f_{DPOSS} = \frac{M_{DPOSS}/\rho_{DPOSS}}{M_{PS}/\rho_{PS} + M_{BPOSS}/\rho_{BPOSS} + M_{DPOSS}/\rho_{DPOSS}} \quad (3)$$

Preparation of the BPOSS-Br Initiator. To a 50 mL round-bottomed flask equipped with a magnetic stirring bar was added BPOSS-OH (438 mg, 0.50 mmol), DIPEA (258 mg, 2.0 mmol), and 10 mL of freshly dried dichloromethane, and the flask was capped by a rubber septum. With stirring, 124 μL (230 mg, 1.0 mmol) of BIBB was added via a syringe. The solution was further stirred at room temperature for 24 h, before the addition of saturated NH_4Cl aqueous solution to quench the reaction. The mixture was separated, washed with brine and water, dried over Na_2SO_4, and evaporated under vacuum to remove the solvent. The residue was purified by flash chromatography (silica gel, with hexane/DCM = 1/1 volume ratio as the eluent) to afford the product as a white solid (435 mg). Yield: 85%. ^{1}H NMR ($CDCl_3$, 500 MHz, ppm): δ 4.15 (t, J = 6.5 Hz, 2H, −OCH_2−), 1.95 (s, 6H), 1.87 (m, 7H), 1.79 (m, 2H), 0.97 (m, 42H, methyl protons on BPOSS), 0.69 (m, 2H), 0.62 (m, 14H). ^{13}C NMR ($CDCl_3$, 125 MHz, ppm): δ 171.6, 67.9, 55.9, 30.8, 25.8, 25.7, 25.7, 23.9, 23.8, 23.8, 22.6, 22.5, 22.5, 22.1, 8.3. ^{29}Si NMR ($CDCl_3$, 100 MHz, ppm): δ −67.6, −67.9. MS (MALDI-TOF, m/z): calcd. monoisotopic mass for [M·Na]$^+$ ($C_{35}H_{75}BrNaO_{14}Si_8$): 1045.2 Da; found 1045.4 Da.

dx.doi.org/10.1021/ma501017e | *Macromolecules* XXXX, XXX, XXX−XXX

Scheme 1. Synthetic Route of the BPOSS-PS$_n$-DPOSS Asymmetric Giant "Bolaform-like" Surfactants[a]

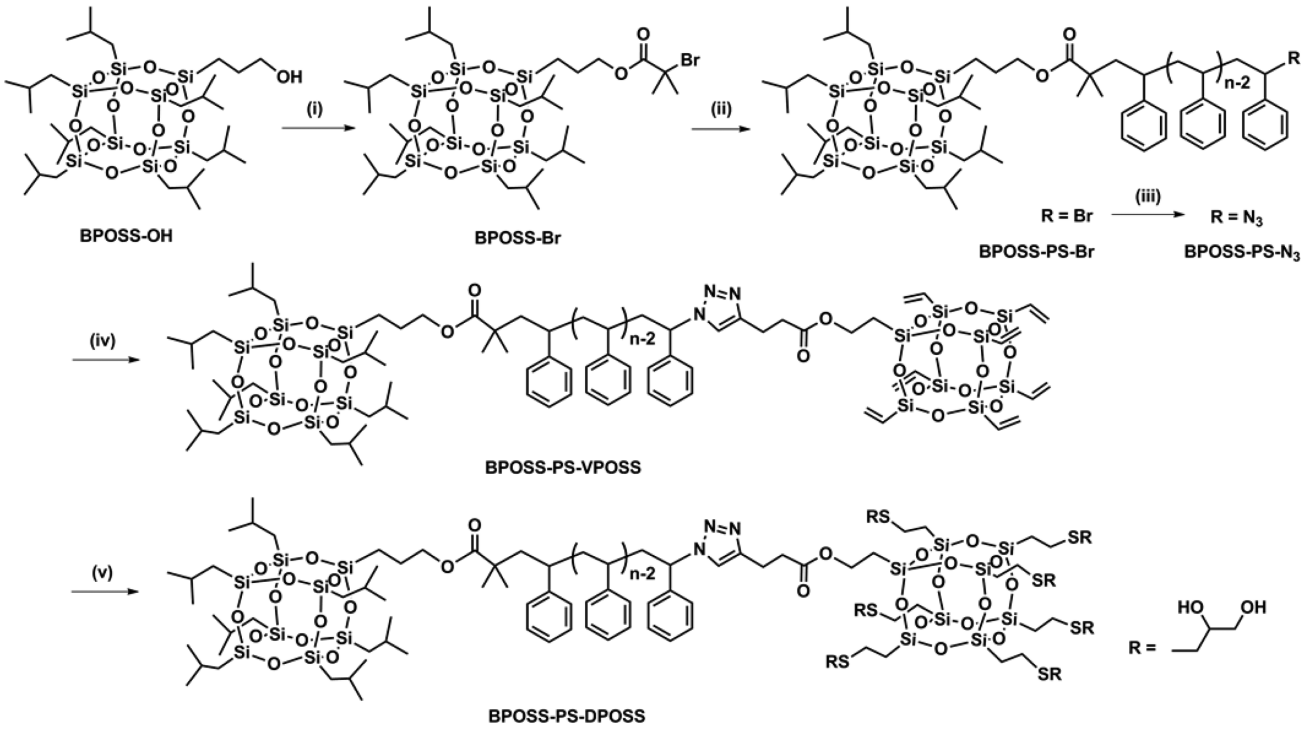

[a]Reagents and conditions: (i) BIBB, DIPEA, CH_2Cl_2, room temperature, 24 h, 85%; (ii) CuBr, PMDETA, styrene, toluene, 110 °C; (iii) NaN_3, DMF, room temperature, 94%; (iv) VPOSS-alkyne, CuBr, PMDETA, toluene, room temperature, 12 h, 80−86%; (v) 1-thioglycerol, Irgacure 2959, THF, *hv*, 15 min, 70−85%.

BPOSS-PS-Br. Polymerization with the BPOSS-Br initiator was conducted similarly according to previous literature with modification.[51] To a 100 mL Schlenk flask equipped with a stirring bar was added BPOSS-Br (103 mg, 0.10 mmol), styrene (10 mL, 87 mmol), CuBr (14 mg, 0.10 mmol), and toluene (10 mL). The mixture was degassed by three freeze−pump−thaw cycles before the addition of PMDETA (21 μL, 0.10 mmol). The mixture was further degassed by one cycle and was then heated to 110 °C to start the polymerization. After the reaction reached a desired conversion, it was quenched by cooling in ice water, and the solution was directly transferred onto a silica gel column. THF was used to wash the product off, and the product was obtained as a white solid by precipitation into methanol two times, followed by vacuum drying overnight. Typical monomer conversions were controlled below 15%. For the sample BPOSS-PS-Br used in the demonstrative synthesis: ^{1}H NMR ($CDCl_3$, 500 MHz, ppm): δ 7.40−6.40 (m, 190H), 4.50 (m, 1H), 3.40 (m, 2H), 2.60−1.30 (m, 128H), 1.02 (m, 42H, methyl protons on BPOSS), 0.66 (m, 14H), 0.56 (m, 2H). ^{13}C NMR ($CDCl_3$, 125 MHz, ppm): δ 177.2, 146.0−145.1, 128.6−125.4, 65.9, 52.4, 46.4−39.8, 30.3, 27.2, 25.7, 23.9, 22.5, 21.9, 8.3 (shown in Figure S1a of the Supporting Information, SI). FT-IR (KBr) ν (cm^{-1}): 3082, 3061, 3027, 2954, 2926, 2870, 1945, 1874, 1805, 1728, 1602, 1493, 1453, 1367, 1331, 1229, 1115 (Si−O−Si asymmetric stretching), 1070, 1030, 909, 838, 757, 700, 541 (shown in Figure S2a). MS (MALDI-TOF, *m*/*z*): calcd monoisotopic mass for $[35mer\cdot Na\text{-}HBr]^+$ ($C_{315}H_{354}NaO_{14}Si_8$): 4607.5 Da; found 4607.8 Da. $M_{n,NMR}$ = 5.0 kg/mol. SEC results: $M_{n,SEC}$ = 5.0 kg/mol, $M_{w,SEC}$ = 5.2 kg/mol, $Đ$ = 1.05.

BPOSS-PS$_{38}$-N$_3$. BPOSS-PS$_{38}$-Br ($M_{n,NMR}$ = 4.5 kg/mol, $Đ$ = 1.05, 300 mg, 0.067 mmol) and sodium azide (65 mg, 1 mmol) were mixed in 5 mL of DMF. The resulting mixture was stirred at room temperature for 24 h. The mixture was washed with water, dried over Na_2SO_4, and evaporated in vacuo. The crude product was purified by precipitation into methanol for two times and collected by vacuum filtering as a white solid (280 mg). Yield: 94%. For the sample BPOSS-PS$_{38}$-N$_3$ used in the demonstrative synthesis: ^{1}H NMR ($CDCl_3$, 500 MHz, ppm): δ 7.40−6.40 (m, 190H), 4.00 (m, 1H), 3.40 (m, 2H), 2.60−1.30 (m, 128H), 1.02 (m, 42H, methyl protons on BPOSS), 0.66 (m, 14H), 0.56 (m, 2H). ^{13}C NMR ($CDCl_3$, 125 MHz, ppm): δ 177.2, 146.0−145.1, 128.6−125.4, 65.9, 64.1, 46.4−39.8, 29.7, 27.2, 25.7, 23.9, 22.5, 21.9, 8.3 (shown in Figure S1b). FT-IR (KBr) ν (cm^{-1}): 3061, 3027, 2926, 2866, 2095 (azide group), 1945, 1872, 1804, 1728, 1602, 1493, 1452, 1367, 1331, 1230, 1113 (Si−O−Si asymmetric stretching), 1030, 909, 838, 754, 700, 541 (shown in Figure S2b). $M_{n,NMR}$ = 5.0 kg/mol. SEC results: $M_{n,SEC}$ = 5.0 kg/mol, $M_{w,SEC}$ = 5.2 kg/mol, $Đ$ = 1.05.

BPOSS-PS$_{38}$-VPOSS. The reaction was performed similarly as previously described.[50] To a 100 mL Schlenk flask equipped with a magnetic stirring bar were added VPOSS-alkyne (40 mg, 0.055 mmol, 1.0 equiv), BPOSS-PS$_{38}$-N$_3$ (M_n = 4.5 kg/mol, $Đ$ = 1.05, 250 mg, 1.0 equiv), CuBr (1 mg, 0.007 mmol, 0.1 equiv), and freshly distilled toluene (30 mL). The resulting solution was degassed by three freeze−pump−thaw cycles before adding PMDETA (10 mg, 12 μL, 1.0 equiv) via a pipet. The mixture was further degassed by one cycle and was then stirred at room temperature for 12 h. After the reaction was completed, the solution was directly transferred onto a silica gel column. Toluene was first used as the eluent to fully remove the unreacted starting materials, and then a mixture of toluene and ethyl acetate (v/v = 1/1) was used to wash the product off the column. After removing the solvent, the crude product was precipitated into cold MeOH and collected by vacuum filtration once and dried under vacuum to afford BPOSS-PS$_{38}$-VPOSS as a white powder (249 mg). Yield: 86%. For the sample BPOSS-PS$_{38}$-VPOSS used in the demonstrative synthesis: ^{1}H NMR ($CDCl_3$, 500 MHz, ppm): δ 7.40−6.40 (m, 191H), 6.20−5.90 (m, 21H, vinyl protons), 5.05 (m, 1H), 4.25 (m, 2H), 3.40 (m, 2H), 2.95 (m, 2H), 2.64 (m, 2H), 2.40−1.40 (m, 128H), 1.35 (m, 2H), 1.03 (m, 42H), 0.68 (m, 14H), 0.55 (m, 2H). ^{13}C NMR ($CDCl_3$, 125 MHz, ppm): δ 177.2, 172.6, 146.0−145.1, 137.0, 128.8−125.4, 120.2, 65.9, 60.7, 46.4−39.8, 33.7, 25.7, 23.8, 22.5, 21.9, 20.9, 13.1, 8.3 (shown in Figure S1c). FT-IR (KBr) ν (cm^{-1}): 3061, 3027, 2930, 2924, 1944, 1872, 1804, 1732, 1602, 1493, 1452, 1406, 1367, 1331, 1276, 1229, 1117 (Si−O−Si asymmetric stretching), 1030, 971, 908, 838, 758, 700, 582, 541 (shown in Figure

dx.doi.org/10.1021/ma501017e | *Macromolecules* XXXX, XXX, XXX−XXX

S2c). MS (MALDI-TOF, m/z): calcd monoisotopic mass for [35mer·Na]$^+$ ($C_{336}H_{385}N_3NaO_{28}Si_{16}$): 5380.5 Da; found 5379.9 Da. $M_{n,NMR}$ = 5.7 kg/mol. SEC: $M_{n,SEC}$ = 5.5 kg/mol, $M_{w,SEC}$ = 5.7 kg/mol, $Đ$ = 1.04.

BPOSS-PS$_{38}$-DPOSS. This reaction was performed similarly as previously described.[50] To an open vial without stirring bar were added BPOSS-PS$_{38}$-VPOSS (M_n = 5.2 kg/mol, $Đ$ = 1.04, 104 mg, 0.020 mmol), 1-thioglycerol (22 mg, 0.20 mmol), the photoinitiator Irgacure 2959 (1 mg, 0.0045 mmol, 0.2 0 equiv per polymer chain, or 0.03 equiv per vinyl group), and a minimum amount of THF (about 2 mL) to fully dissolve the solids. The reaction was complete after irradiation by 365 nm UV light for 15 min. The mixture was purified by repeated precipitation from concentrated THF solutions of the crude products into MeOH/water mixture (v/v = 1/1). After two precipitations and subsequent drying, the product was collected as a white solid (96 mg). Yield: 80%. For the sample BPOSS-PS$_{38}$-DPOSS used in the demonstrative synthesis: ^{1}H NMR ($CDCl_3$, 500 MHz, ppm): δ 7.40−6.40 (m, 191H), 5.05 (m, 1H), 4.18 (m, 2H), 4.05−3.30 (m, 23H), 3.10−2.50 (m, 32H) 2.40−1.40 (m, 128H), 1.35−1.03 (m, 58H), 0.68 (m, 14H), 0.55 (m, 2H). ^{13}C NMR ($CDCl_3$, 125 MHz, ppm): δ 145.6−145.1, 128.3−127.5, 125.6−125.5, 77.3, 77.1, 76.8, 71.2, 65.9, 65.4, 45.9, 44.5−43.9, 42.8, 42.0, 41.6, 40.6−40.1, 35.2, 34.3, 30.4, 26.7, 25.7, 23.9, 22.5, 22.5, 21.9, 20.9, 8.4 (shown in Figure S1d). FT-IR (KBr) ν (cm^{-1}): 3391, 3061, 3027, 2925, 2246, 1943, 1873, 1800, 1733, 1602, 1494, 1450, 1367, 1285, 1202, 1147, 1113 (Si−O−Si asymmetric stretching), 1029, 955, 910, 837, 736, 700, 650, 557, 538 (shown in Figure S2d). $M_{n,NMR}$ = 6.5 kg/mol. SEC: $M_{n,SEC}$ = 7.0 kg/mol, $M_{w,SEC}$ = 7.3 kg/mol, $Đ$ = 1.04.

RESULTS AND DISCUSSION

Synthesis of BPOSS-PS$_n$-DPOSS. Asymmetrically MNP-tethered polymers are intriguing targets of the proposed giant surfactant library.[42] Introduction of two POSS cages with different functionalities provides the platform to study how the different functional groups on the POSS cages would affect the self-assembly behaviors. The synthetic route of a model sample BPOSS-PS$_{38}$-DPOSS is illustrated in Scheme 1. Chemical modifications of BPOSS derivatives to introduce functional groups suitable for various controlled polymerization methods, such as ATRP[54] and reversible addition−fragmentation chain transfer polymerization (RAFT),[35] have been reported. ATRP was chosen since it gives high chain-end functionality and the chain ends can be facilely converted to azide group for copper-catalyzed azide−alkyne [3 + 2] cycloaddition (CuAAC) reaction.[55,56] The structure of this new initiator BPOSS-Br was confirmed by NMR and MALDI-TOF MS spectrometry. All the resonance peaks in the ^{1}H and ^{13}C NMR spectra can be assigned, as shown in Figure 1a,b. Because of the asymmetric structures of BPOSS-Br, the isobutyl groups show three different sets of peaks in ^{13}C NMR spectrum (see Figure 1b, inset). The ^{29}Si NMR spectrum of BPOSS-Br shows two peaks (Figure 1c), corresponding to the two different kinds of silicon atoms with different substituted groups in BPOSS-Br.[46,57] Furthermore, the observed m/z ratio in MS spectrum agrees well with the calculated value (1045.4 Da vs 1045.2 Da, see Figure 1d). All these characterization data clearly proved the structure and purity of the BPOSS-Br initiator.

ATRP of styrene in toluene at 110 °C results in polymers with different molecular weights and a narrow molecular weight distribution ($Đ$ < 1.10).[58] One representative BPOSS-PS-Br polymer with a degree of polymerization N = 38 was fully characterized by ^{1}H NMR (Figure 2a), ^{13}C NMR (Figure S1a), FT-IR (Figure S2a), SEC (Figure 3), and MALDI-TOF (Figure 4a) techniques, and all the results confirmed the precise structure of this polymer. It is noteworthy that the MS data of the BPOSS-PS$_{38}$-Br were obtained with monoisotopic resolution. The observed m/z value is in very good agreement with the calculated value corresponding to the desired product with one HBr molecule eliminated and ionized with sodium ion (see Figure 4a). This phenomenon is commonly observed in ω-bromo-functionalized PS.[59]

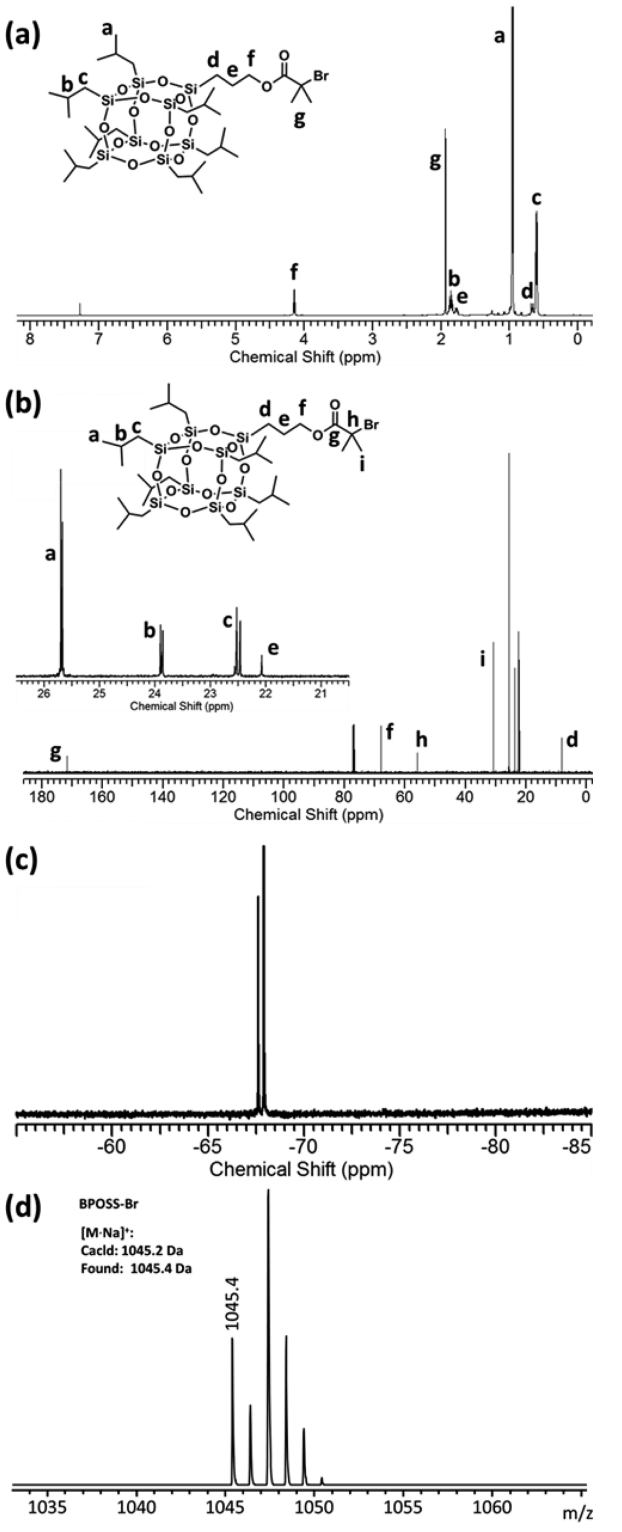

Figure 1. (a) ^{1}H NMR spectrum, (b) ^{13}C NMR spectrum (with zoom-in view), (c) ^{29}Si NMR spectrum, and (d) MALDI-TOF MS spectrum of the BPOSS-Br initiator.

dx.doi.org/10.1021/ma501017e | Macromolecules XXXX, XXX, XXX−XXX

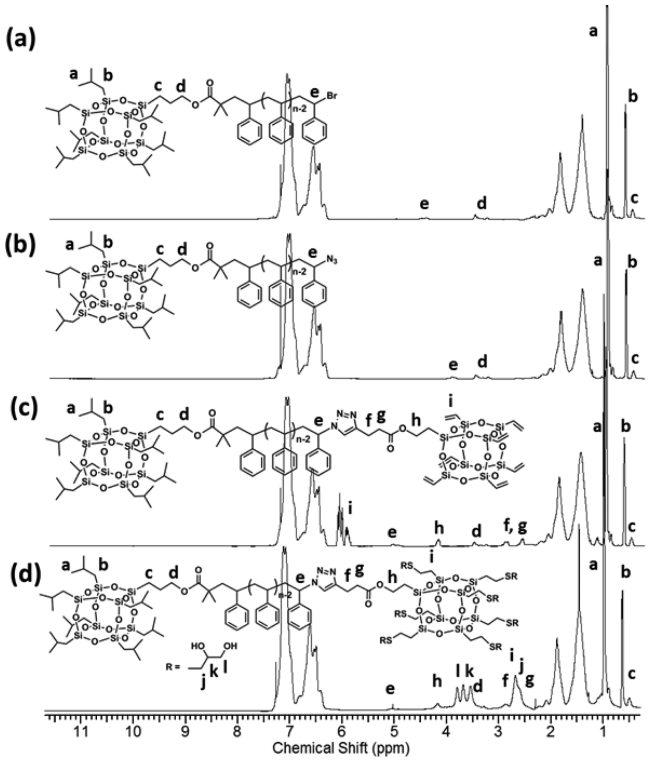

Figure 2. ^{1}H NMR spectra of (a) BPOSS-PS$_{38}$-Br, (b) BPOSS-PS$_{38}$-N$_3$, (c) BPOSS-PS$_{38}$-VPOSS, and (d) BPOSS-PS$_{38}$-DPOSS.

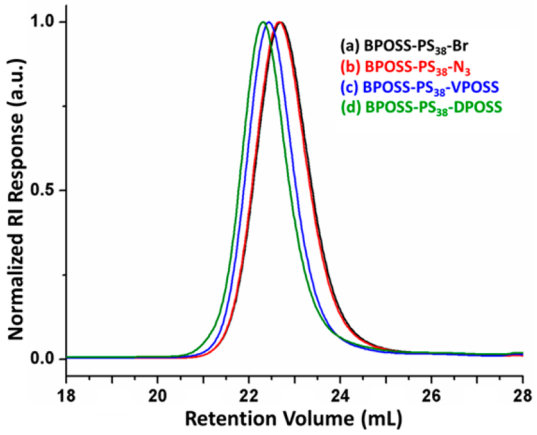

Figure 3. SEC overlay of (a) BPOSS-PS$_{38}$-Br (black curve), (b) BPOSS-PS$_{38}$-N$_3$ (red curve), (c) BPOSS-PS$_{38}$-VPOSS (blue curve), and (d) BPOSS-PS$_{38}$-DPOSS (green curve).

Subsequent nucleophilic substitution reaction of BPOSS-PS$_{38}$-Br with sodium azide successfully transformed the bromo into azide. Because of the instability of azide group, we were unable to obtain a clean MALDI-TOF mass spectrum for BPOSS-PS$_{38}$-N$_3$.[45] Nevertheless, the strong new vibrational band in the FT-IR spectrum at ~2095 cm^{-1} (see Figure S2b) and the downfield shift of the proton resonance signal adjacent to the azide group compared to the same proton in BPOSS-PS$_{38}$-Br (4.50 to 4.00 ppm, proton **e** in Figure 2a,b) in ^{1}H NMR spectrum clearly support the formation of BPOSS-PS$_{38}$-N$_3$.[50,60] SEC trace of BPOSS-PS$_{38}$-N$_3$ (Figure 3) is monomodal and narrow, essentially the same as BPOSS-PS$_{38}$-Br since the modification occurs only at the chain end. Therefore, the structure of BPOSS-PS$_{38}$-N$_3$ is confirmed, and it was then

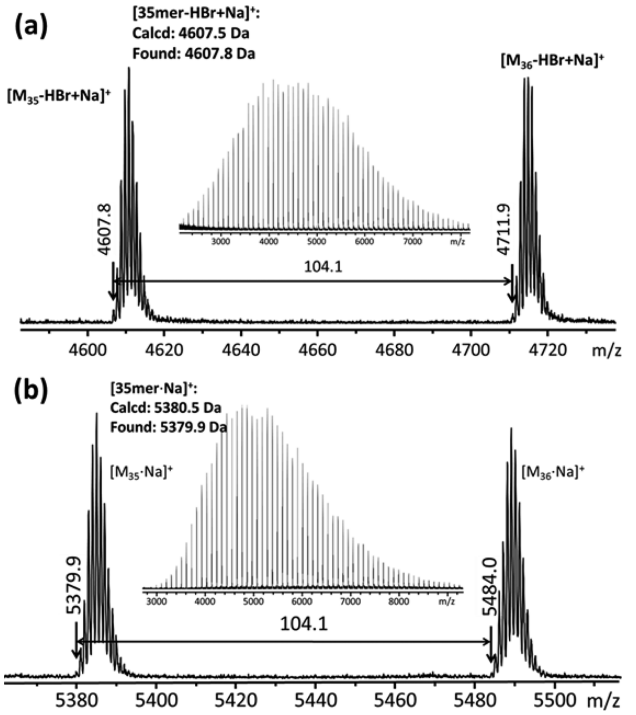

Figure 4. MALDI-TOF mass spectra of (a) BPOSS-PS$_{38}$-Br and (b) BPOSS-PS$_{38}$-VPOSS. Both spectra were acquired with monoisotopic resolution. The insets show the full spectrum.

subjected to react with VPOSS-alkyne following the sequential click approach.[44,45,50]

The reported sequential "click" approach is well compatible with the BPOSS-PS$_{38}$-N$_3$.[50] Under similar reaction conditions, the chemical conjugation of VPOSS-alkyne with the BPOSS-PS$_{38}$-N$_3$ can be successfully achieved via the CuAAC reaction.[55,56,61] Purification by flash column chromatography and precipitation into cold methanol afford BPOSS-PS$_{38}$-VPOSS as a white solid in good yield. Molecular characterizations substantiate the structure of BPOSS-PS$_{38}$−VPOSS. In the ^{1}H NMR spectrum, the newly appearing resonance signals can all be assigned, among which the characteristic vinyl shifts show up again at 6.20−5.90 ppm. FT-IR data show complete disappearance of the azide absorbance band (~2095 cm^{-1}), along with an increased relative strength of the Si−O−Si asymmetric stretching band (~1117 cm^{-1}), consistent with the fact that two POSS cages are incorporated into this molecule (see Figure S2c). SEC overlay shown in Figure 3 illustrates a clear shift to the lower retention volume after attaching VPOSS to the ω-end of BPOSS-PS$_{38}$-N$_3$. The MALDI-TOF spectrum (Figure 4b) was obtained with monoisotopic resolution, and the observed m/z ratio is in excellent agreement with the calculated value (see Table 1).

Final modification of BPOSS-PS$_{38}$-VPOSS by thiol−ene "click" reaction[62−64] was performed following the general procedure using 1-thioglycerol as the thiol ligand. After 15 min of UV irradiation, the vinyl proton signals disappeared completely in the ^{1}H NMR spectrum, and the product was simply purified by precipitation into cold methanol/water mixture twice. The product was then thoroughly characterized by ^{1}H NMR (Figure 2d), ^{13}C NMR (Figure S1d), and FT-IR spectrometry (Figure S2). Disappearance of the resonance signals from vinyl group (~6.0 ppm in ^{1}H NMR, 137.0 ppm in ^{13}C NMR) and emergence of the resonance signals from the

dx.doi.org/10.1021/ma501017e | Macromolecules XXXX, XXX, XXX−XXX

Table 1. Summary of Molecular Characterizations of the Polymers Used in the Demonstrative Synthesis

sample	molecular formula	M_{Calcd} (Da)	M_{Found} (Da)	$M_{n,NMR}$[c] (kg/mol)	$M_{n,SEC}$[d] (kg/mol)	$M_{w,SEC}$[d] (kg/mol)	$Đ$[d]
BPOSS-PS_{38}-Br	$C_{315}H_{354}NaO_{14}Si_8$[a]	4607.5[a]	4607.8[a]	5.0	5.0	5.2	1.05
BPOSS-PS_{38}-N_3				5.0	5.0	5.2	1.05
BPOSS-PS_{38}-VPOSS	$C_{336}H_{385}N_3NaO_{28}Si_{16}$[b]	5380.5[b]	5379.9[b]	5.7	5.5	5.7	1.04
BPOSS-PS_{38}-DPOSS				6.5	7.0	7.3	1.04

[a]These data were calculated based on 35mer losing a HBr with a sodium ion ($[35mer - HBr + Na]^+$). [b]These data were calculated based on 35mer with a sodium ion ($[35mer{\cdot}Na]^+$). [c]These data were calculated based on ^{1}H NMR spectra using the integration ratio of the corresponding resonance peaks. [d]These data are obtained from SEC measurements using the PS standards.

Table 2. Summary of the Characterization Data of a Series of BPOSS-PS_n-DPOSS Giant Surfactants

sample	$M_{n,NMR}$[a] (kg/mol)	$Đ$[b]	f_{BPOSS}[c]	f_{PS}[c]	f_{DPOSS}[c]	phase	q_1[d] (nm^{-1})	d_1[d] (nm)
BPOSS-PS_{12}-DPOSS	3.7	1.07	0.29	0.37	0.34	Lam	0.81	7.8
BPOSS-PS_{28}-DPOSS	5.4	1.05	0.19	0.59	0.22	DG	0.70	9.0
BPOSS-PS_{38}-DPOSS	6.5	1.04	0.16	0.66	0.18	Hex	0.66	9.5
BPOSS-PS_{76}-DPOSS	10.4	1.04	0.09	0.80	0.11	Hex	0.58	10.8
BPOSS-PS_{120}-DPOSS	15.0	1.04	0.07	0.85	0.08	BCC	0.57	11.0

[a]These data were calculated based on ^{1}H NMR spectra using the integration ratio of the corresponding resonance peaks. [b]These data are obtained from SEC measurements using the PS standards. [c]These data are calculated based on the molecular weight information from ^{1}H NMR and the density values of the compositional building blocks at room temperature. [d]q_1 is the position of the principal scattering vector, and d_1 is the corresponding principal spacing calculated from q_1.

newly formed thioether linkage (~2.7 ppm in ^{1}H NMR) were direct evidence of the successful reaction. In SEC overlay (Figure 3), it is apparent that the elution profile after functionalization is still narrowly distributed and symmetric. The shift to smaller retention volume is in good agreement with the increased molecular weight. Because of its relatively high molecular weight and heterogeneity in composition, the MALDI-TOF mass spectrum of the final product BPOSS-PS_{38}-DPOSS was not obtained in good quality. However, all the available evidence strongly supports the completion of the thiol−ene reaction and the formation of the novel molecular architecture of a PS tethered with two chemically distinct POSS cages, one at each chain end. The resulting materials are then subject to self-assembly studies.

It is known that the volume fraction of each polymer block dominates the formation of various ordered structures, as demonstrated in linear diblock copolymers.[7,10] In our BPOSS-PS_n-DPOSS system, as the chemical structures of the two POSS cages are precisely defined, the only varying parameter is the molecular weight of the PS chain interconnect. Therefore, to explore the formation of different ordered phases, a series of BPOSS-PS_n-DPOSS samples with different PS chain lengths are prepared via controlling the reaction time in the ATRP step. Five samples are prepared, and their molecular characterization data are summarized in Table 2. The average molecular weights of the products are obtained from ^{1}H NMR analysis with reference to the methyl groups on the periphery of the end-capped BPOSS cages. SEC results confirm that all the BPOSS-PS_n-DPOSS products have very low molecular weight dispersity and precisely defined chemical structures (Figure 5).

Self-Assembly in the Bulk State. Thermal stability of the BPOSS-PS_n-DPOSS samples was first examined by the TGA technique. In the N_2 atmosphere, it is apparent that their weight losses begin at temperatures higher than 200 °C at a scan rate of 10 °C/min (see Figure S3), indicating good thermal stability of the samples. From the DSC results, the glass transitions of the PS chains can be clearly observed during the second heating/cooling cycle. The observed increases of the glass transition temperature (T_g^{PS}) along with the increase of

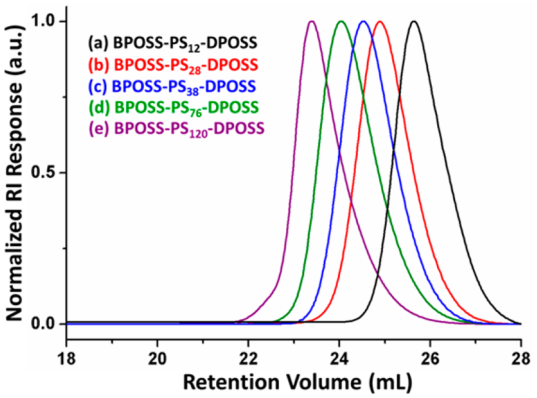

Figure 5. SEC overlay of (a) BPOSS-PS_{12}-DPOSS (black curve), (b) BPOSS-PS_{28}-DPOSS (red curve), (c) BPOSS-PS_{38}-DPOSS (blue curve), (d) BPOSS-PS_{76}-DPOSS (green curve), and (e) BPOSS-PS_{120}-DPOSS (purple curve).

PS interconnect molecular weights show a qualitatively similar trend to the T_g^{PS} value changes in the pure low-molecular-weight linear PS fractions,[65] although the absolute values differ due to the two end-capped POSS cages, especially for the samples with low PS molecular weights.

Considering that the relatively low molecular weights of the PS interconnects in this series of BPOSS-PS_n-DPOSS samples are around or below the critical entanglement length of PS (ca. 25 kg/mol), the thermal annealing process above the T_g^{PS} is sufficient to induce nanophase separation. Similar to our previous study of the DPOSS-PS_n system,[41] the thermal treatment of these bulk BPOSS-PS_n-DPOSS samples was conducted at 150 °C for a few minutes to several hours to achieve the formation of highly ordered phase structures in the bulk samples, as monitored by SAXS experiments. As shown below, the 1D SAXS patterns of all the samples with different molecular weights exhibit sharp principal scattering peaks and higher order peaks after the thermal annealing. From the positions of the principal scattering peaks, the corresponding real space domain spacing d_1 can be calculated according to $d_1 = 2\pi/q_1$. These data are summarized in Table 2.

dx.doi.org/10.1021/ma501017e | Macromolecules XXXX, XXX, XXX−XXX

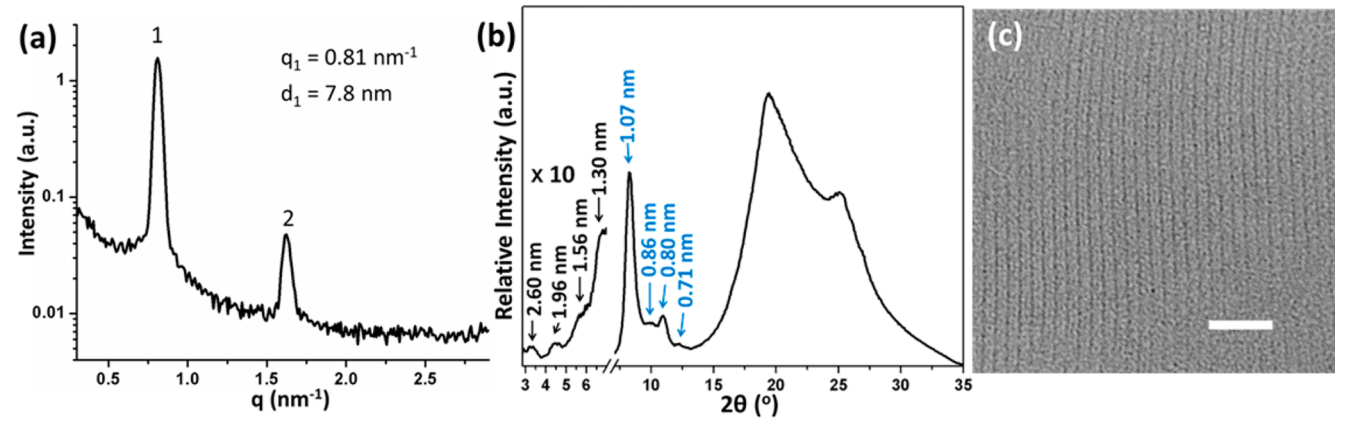

Figure 6. (a) 1D SAXS profile and (b) 1D WAXD pattern of BPOSS-PS$_{12}$-DPOSS recorded after the thermal treatment. The black arrows in (b) indicate the higher order scattering peaks of the self-assembled Lam structure, while the blue arrows indicate the diffraction peaks from crystalline BPOSS moieties. The halo at high angle region comes from the PS interconnects. (c) TEM bright-field image of microtomed BPOSS-PS$_{12}$-DPOSS sample without staining. The scale bar is 40 nm.

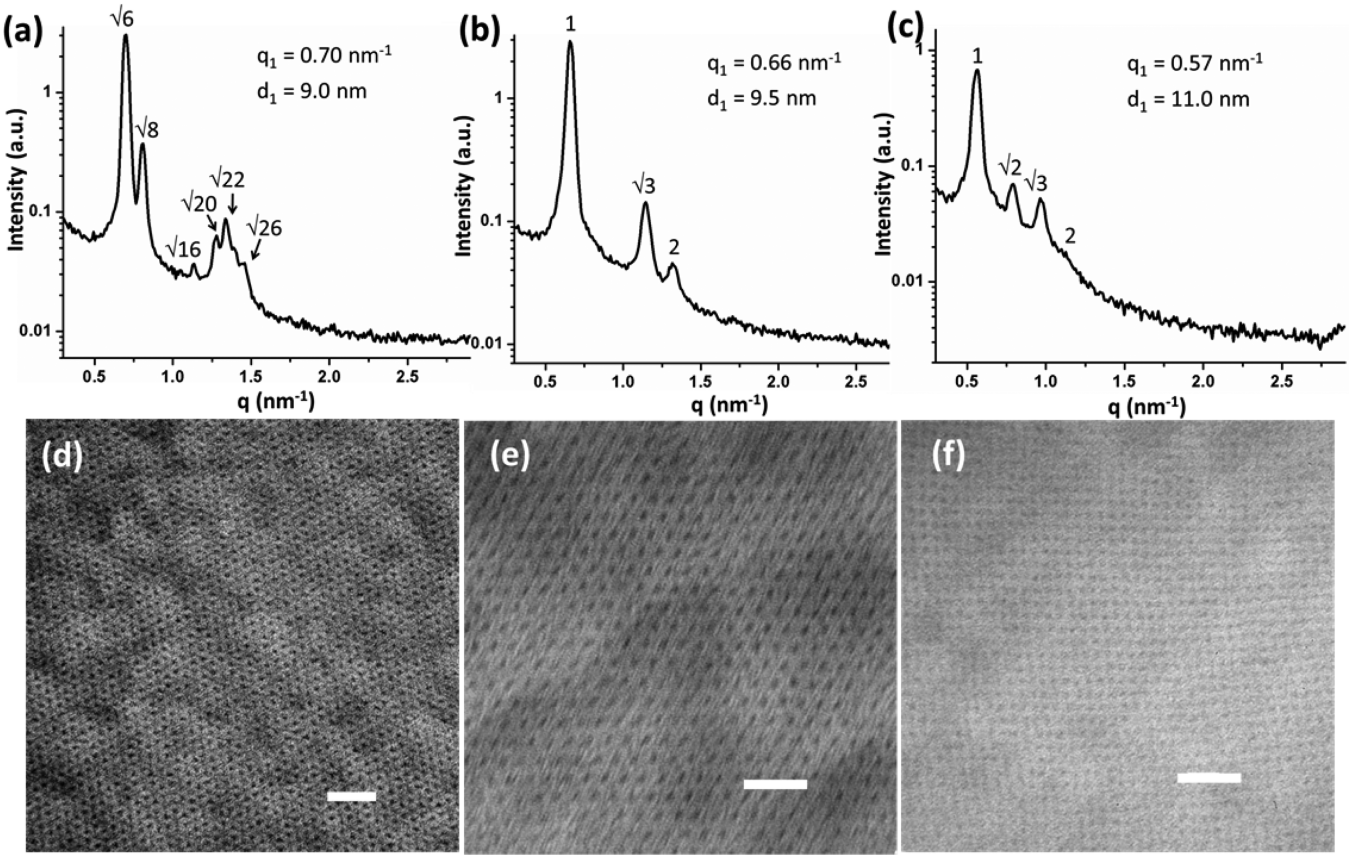

Figure 7. 1D SAXS profiles of (a) BPOSS-PS$_{28}$-DPOSS, (b) BPOSS-PS$_{38}$-DPOSS, and (c) BPOSS-PS$_{120}$-DPOSS. Bright-field TEM images of (d) BPOSS-PS$_{28}$-DPOSS, (e) BPOSS-PS$_{38}$-DPOSS, and (f) BPOSS-PS$_{120}$-DPOSS. Scale bar: 40 nm.

First, the BPOSS-PS$_{12}$-DPOSS sample with the shortest PS interconnect among the samples forms a Lam nanostructure after the thermal annealing. Two scattering peaks can be observed in the SAXS pattern shown in Figure 6a, with the q/q_1 ratio of 1:2. Notably, the periodic spacing calculated from the primary peak (centered at q_1 = 0.81 nm^{-1}) in SAXS data is 7.8 nm. 1D WAXD data of the thermally treated BPOSS-PS$_{12}$-DPOSS bulk sample in Figure 6b shows several sharp diffraction peaks at a 2θ region between 7° and 15°, along with the broad halos in the higher 2θ region. The two strong diffraction peaks located at 2θ = 8.3° and 11.1° (blue arrows in Figure 6b) are characteristic diffraction peaks attributed to the crystalline BPOSS moieties,[66] indicating that the BPOSS cages in the self-assembled Lam structure are crystallized and separated from the PS domains. In addition, four weak scattering peaks in the 2θ region below 7° are also observed, which can be assigned as the higher order scattering peaks from the Lam structure (black arrows in Figure 6b). The *d*-spacings in the real space are 2.6, 1.96, 1.56, and 1.3 nm, respectively, matching well with the third, fourth, fifth, and sixth order peaks

dx.doi.org/10.1021/ma501017e | *Macromolecules* XXXX, XXX, XXX−XXX

of the primary scattering peak in the SAXS pattern. The broad halo centered at around 20.0° is assigned to the average lateral distance of the PS interconnects.[37]

TEM bright-field image of the microtomed sample in Figure 6c shows alternative dark and gray line domains without staining, confirming the self-assembled Lam structure. The thickness of the dark domain is measured to be ~2.6 nm, while that of the gray domains is ~5.2 nm. Since the DPOSS cages bearing hydroxyl groups can be stained by osmium tetroxide, we also carried out the staining process to prove that the dark domains are indeed the hydrophilic DPOSS domains (Figure S4). Careful examination of the TEM image in Figure 6c identifies a slightly darker line at the middle of the gray domains between every two dark DPOSS domains. We speculate that they may be attributed to the crystalline BPOSS domains. Considering the similar sizes of the BPOSS and DPOSS cages, it is proposed that the BPOSS cages form a double layered 2D crystalline sheet in between two neighboring PS domain.[53] For BPOSS-PS_{12}-DPOSS, the calculated f_{DPOSS} based on the density is 0.34, matching with the thickness values of the alternating lamellae domains observed in the TEM image (Figure 6c). The fact that the DPOSS domains occupy about one-third of the domain volume also explains the relatively low intensity of the third-order scattering peak in the SAXS pattern, partly due to distinction.

The self-assembled structure changes when the length of the PS interconnects increases to 28 repeating units. Figure 7a shows the 1D SAXS pattern of the BPOSS-PS_{28}-DPOSS sample, from which multiple scattering peaks with the q/q_1 ratio of $\sqrt{6}:\sqrt{8}:\sqrt{16}:\sqrt{20}:\sqrt{22}:\sqrt{26}$ can be observed, revealing a highly ordered DG structure.[67] The distance d_1 calculated from the primary peak is 9.0 nm. Figure 7d is a TEM bright-field image of the microtomed BPOSS-PS_{28}-DPOSS sample that exhibits the characteristic "wagon wheel" pattern along the [111] direction, confirming the DG structure.[67] The corresponding 1D WAXD pattern of BPOSS-PS_{28}-DPOSS, however, does not show any sharp diffraction peaks in the 2θ angle region larger than 4°, except two broad scattering halos (Figure S5a). The halo centered at around 9.3° is attributed to the average distances between the POSS cages. The lack of sharp diffraction peaks in the WAXD data suggests that in the self-assembled DG phase the BPOSS cages are not able to crystallize and be phase-separated from the PS domains, presumably due to hindrance of the curved interfaces between the phase-separated domains.

Further increasing the length of the PS chains leads to the formation of a Hex structure. Two samples, BPOSS-PS_{38}-DPOSS and BPOSS-PS_{76}-DPOSS with f_{DPOSS} values being 0.18 and 0.11, respectively, are found to be located in the Hex phase region. The q/q_1 ratios of the two 1D SAXS patterns (Figure 7b and Figure S6) are $1:\sqrt{3}:2$, revealing the characteristic pattern of the Hex phase for both samples. The corresponding interplanar spacing d_1 values calculated from q_1 are 9.5 nm for BPOSS-PS_{38}-DPOSS and 10.8 nm for BPOSS-PS_{76}-DPOSS. Hexagonally packed cylinders can also be clearly observed from the TEM bright-field image of a microtomed BPOSS-PS_{38}-DPOSS sample that was cut along the normal direction to the long axis of the cylinders (viewing along the [000l] direction) as shown in Figure 7e. Based on the TEM image, it can be recognized that the cylindrical domains are composed of the DPOSS moieties, while the PS and the BPOSS cages together form the matrix. Moreover, the cylinder radius (D_c) can be calculated according to eq 4:

$$D_c = [(2f_{DPOSS}d_1^2)/(\sqrt{3}\pi)]^{1/2} \quad (4)$$

For BPOSS-PS_{38}-DPOSS, f_{DPOSS} = 0.18, the calculated D_c is 2.4 nm, matching well with the estimated values observed in the TEM images (2.3 ± 0.2 nm for BPOSS-PS_{38}-DPOSS). The 1D WAXD patterns (Figure S5b,c) of these two samples show no sharp diffractions but only two broad halos in the 2θ angle region above 4° in each case, suggesting that BPOSS cages are not crystalline in the Hex structures.

Figure 7c shows a 1D SAXS profile of BPOSS-PS_{120}-DPOSS that possesses four scattering peaks with q/q_1 ratio of $1:\sqrt{2}:\sqrt{3}:2$, indicating the formation of a BCC phase with calculated d_1 being 11.0 nm. The BCC phase is also confirmed by the TEM bright-field image (Figure 7f) along the [100] direction. As the minor domain in its volume fraction, the DPOSS cages forms the spherical cores and the BPOSS and PS are in the matrix. For the BCC phase, the radius of the spheres (D_s) can be calculated from volume fraction of the minor blocks according to eq 5:

$$D_s = [(3f_{DPOSS}d_1^3)/(\sqrt{8}\pi)]^{1/3} \quad (5)$$

Again, comparison of the calculated value of 3.2 nm and experimentally observed data (3.0 ± 0.1 nm) gives rise to the matched results. This indicates that only hydroxyl-group-functionalized DPOSS nanoparticles possess strong enough interaction parameter to nanophase separate from the PS domains. The 1D WAXD pattern (Figure S5d) again shows no sharp diffractions but only broad halos, suggesting that BPOSS cages are not crystalline in the BCC structures. A summary of the characterization data is shown in Table 2.

Molecular Packing Model and Phase Diagram. From the experimental observations presented above, it can be concluded that the BPOSS-PS_n-DPOSS conjugates can be considered as one particular realization of amphiphilic molecules exhibiting self-assembled lamellar, gyroidal, cylindrical, and spherical phases. The self-assembly or nanophase separation is driven by the incompatibility between the hydrophilic DPOSS cages and the hydrophobic PS interconnects and BPOSS cages, whereas the type of ordered phases is determined by the volume fraction of the hydrophilic and hydrophobic parts. When the BPOSS cages are amorphous, this scenario is similar to the other amphiphilic diblock copolymers[7,10] and the DPOSS-PS_n conjugates.[41] In particular, in the ordered phases with curved domain interfaces (DG, Hex, and BCC), crystallization of BPOSS cages is suppressed due to the packing constraint, and thus, the BPOSS cages are mixed within the PS chains to maximize entropy to form the hydrophobic domain.

On the other hand, the nanophase-separated Lam structure observed from the BPOSS-PS_{12}-DPOSS sample is characterized by planar interfaces. The BPOSS cages in the lamellae of BPOSS/PS domains can crystallize within a 1D confinement[68] with flat interfaces, and thus, crystallization of BPOSS cages demonstrates a "crystallization-induced nanophase separation" phenomenon. Without the 1D confinement, a BPOSS-PS_{28}-Br sample with similar BPOSS volume fraction results in certain aggregates of BPOSS cages, and therefore, only broad diffraction halos can be observed in WAXD patterns (see Figure S7). Similar WAXD results have also been reported in another BPOSS-PS_n conjugate system.[34] The Lam structure is schematically illustrated in Figure 8, where the nanophase separation between the hydrophilic DPOSS cages and the

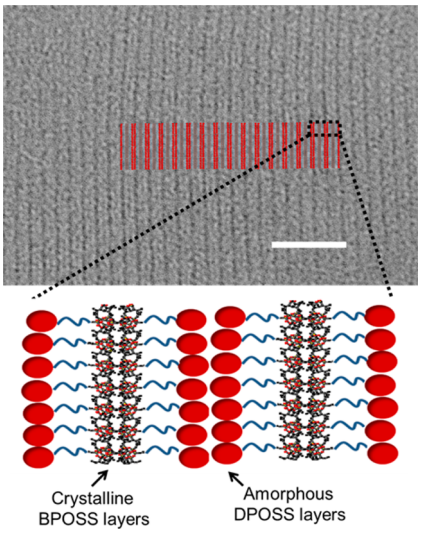

Figure 8. Schematic illustration of the Lam structure formed by BPOSS-PS_{12}-DPOSS. Scale bar: 40 nm.

hydrophobic PS/BPOSS cages generates the primary Lam structure (the red double layers on the TEM image of Figure 8). Within the hydrophobic domains, the BPOSS cages further form crystalline regions (between two red double layers on the TEM image of Figure 8), driven by the interactions among BPOSS cages (enthalpy) which outweigh the entropic maximization. The cross-section area of each BPOSS-PS_{12}-DPOSS at the interfaces between the alternative lamellae domains can be estimated by eq 6

$$A = \frac{2M_{\mathrm{DPOSS}}}{\rho_{\mathrm{DPOSS}} N_{\mathrm{A}} d_1 f_{\mathrm{DPOSS}}} \tag{6}$$

where M_{DPOSS} is the molar mass of the DPOSS segment and N_{A} is the Avogadro constant. For BPOSS-PS_{12}-DPOSS, the calculated value of A is 1.31 nm^2, which is reasonable considering the size of the DPOSS cages.

Although a semiquantitative analysis of the molecular packing in the DG phase is complicated due to the fact that the interfaces are convoluted with nonuniform curvatures, a semiquantitative analysis of the molecular packing can be carried out for the Hex phase. Specifically, we can calculate the average number of giant "bolaform-like" surfactants in each cross section of the columns composed of DPOSS cages.[69] The unit height of the column h, estimated from the center of the first broad halo in the WAXD diffraction patterns of BPOSS-PS_{38}-DPOSS and BPOSS-PS_{76}-DPOSS, is 0.90 nm (see Figure S5b,c). Therefore, the number of molecules per cylinder stratum in the Hex phase can be calculated by eq 7

$$\mu = \frac{2d_1^{\,2}h}{\sqrt{3}\,V_0} = \frac{2d_1^{\,2}hN_{\mathrm{A}}}{\sqrt{3}\,(M_{\mathrm{PS}}/\rho_{\mathrm{PS}} + M_{\mathrm{BPOSS}}/\rho_{\mathrm{BPOSS}} + M_{\mathrm{DPOSS}}/\rho_{\mathrm{DPOSS}})} \tag{7}$$

where V_0 is the average volume of one BPOSS-PS_n-DPOSS molecule. For BPOSS-PS_{38}-DPOSS, the average number per cylinder stratum is 10, while for BPOSS-PS_{76}-DPOSS, it decreases to about 8. If we consider the overall shape of a single molecule in the Hex phase as a fan-shaped sector, the decreased number of molecules per cylinder stratum indicates increased planar angle of each sector, due to the increased volume fraction of the PS/BPOSS matrix. The angles of the fan-shaped sector corresponding to a single macromolecule in the cylinders for BPOSS-PS_{38}-DPOSS and BPOSS-PS_{76}-DPOSS are calculated as 36° and 45°, respectively. Similarly, the number of giant "bolaform-like" surfactants in one aggregated DPOSS sphere[70] can be calculated by eq 8:

$$\mu = \frac{\sqrt{2}\,d_1^{\,3}}{V_0} = \frac{\sqrt{2}\,d_1^{\,3}N_{\mathrm{A}}}{M_{\mathrm{PS}}/\rho_{\mathrm{PS}} + M_{\mathrm{BPOSS}}/\rho_{\mathrm{BPOSS}} + M_{\mathrm{DPOSS}}/\rho_{\mathrm{DPOSS}}} \tag{8}$$

For BPOSS-PS_{120}-DPOSS, the value of μ is 82, and the projection of the solid angle of each cone composing the sphere is thus about 4.4°.[69,70]

An estimated phase diagram of the BPOSS-PS_n-DPOSS system can be constructed based on the experimental observations. As mentioned above, phase behavior is controlled by the total volume fraction of the hydrophobic components, $f_{\mathrm{BPOSS+PS}}$ (which equals to $f_{\mathrm{BPOSS}} + f_{\mathrm{PS}}$), or, equivalently, by the volume fraction of the hydrophilic component, f_{DPOSS} (which equals to $1 - f_{\mathrm{BPOSS+PS}}$). From the ordered phases of the five examples examined in this study (Table 2), the phase boundary between the different ordered phases can be assessed. For example, it can be estimated that the lamellar to gyroidal transition occurs around $f_{\mathrm{DPOSS}} = 0.22$; the gyroidal to cylindrical transition occurs between $f_{\mathrm{DPOSS}} = 0.22$ and 0.18; the cylindrical to spherical transition occurs between $f_{\mathrm{DPOSS}} = 0.11$ and 0.08. In our previous study of the DPOSS-PS system,[41] the corresponding phase boundaries are estimated to be $f_{\mathrm{DPOSS}} = 0.22$, 0.21, and 0.10. The estimated phase boundaries of the DPOSS-PS_n-BPOSS system are in good agreement with those of the DPOSS-PS system.[41]

An interesting case is the extreme situation where $N_{\mathrm{PS}} = 0$, the resulting molecule BPOSS-DPOSS is similar to one example of our previously reported POSS-based molecular Janus nanoparticles.[53] It has been established that the comparable sizes of BPOSS and DPOSS cages and chemical incompatibility induced by the different functional groups lead to the formation of a Lam supramolecular phase for BPOSS-DPOSS.[53] Therefore, the lowest limit of the lamellar phase is at $f_{\mathrm{BPOSS+PS}} = 0.46$ or $f_{\mathrm{DPOSS}} = 0.54$ (at the limit of $f_{\mathrm{PS}} = 0$, calculated from the BPOSS-DPOSS molecule).

Comparing with the phase behavior of linear diblock copolymers, the phase boundaries of the DPOSS-PS_n-BPOSS conjugates shift to smaller f_{DPOSS} values.[7] This behavior is similar to the DPOSS-PS_n system.[41] The shifted phase boundary compared with symmetric diblock copolymers is explained by the conformational rigidity of the DPOSS cages, which resulted in increased "effective cross-section areas" at the interfaces.[41,71,72] As a result, to form phases with more curved interfaces (e.g., Lam to DG, or Hex to BCC), the volume fraction of the PS and BPOSS domains should be larger to introduce high enough interfacial curvature. Furthermore, the fact that the BPOSS cages could crystallize in the lamellar phase changes the behavior of the DPOSS-PS_n-BPOSS conjugates as compared with the DPOSS-PS samples. This observation indicates that the interactions between, and the packing of, the POSS cages with different functional groups and the PS interconnects play a subtle role in the determination of the equilibrium morphology of the self-assembled structures.

dx.doi.org/10.1021/ma501017e | *Macromolecules* XXXX, XXX, XXX–XXX

CONCLUSIONS

To summarize, the design, synthesis, and self-assembly behaviors of a set of asymmetric giant "bolaform-like" surfactants, which are composed of one PS interconnect tethered with two differently functionalized POSS cages at both PS ends, are reported. The synthesis combined a "growth-from" strategy and a sequential "click" approach to prepare the precisely defined surfactants that are fully characterized by ^{1}H and ^{13}C NMR, FT-IR, SEC, and MALDI-TOF mass spectroscopy. After thermal annealing at 150 °C, the BPOSS-PS$_n$-DPOSS samples with different PS molecular weights are found to form different ordered structures (Lam, DG, Hex, and BCC) with feature sizes of 10 nm or less, depending on the volume fraction of the DPOSS domain. The driving force toward nanophase separation is the chemical incompatibility between the hydrophilic DPOSS cages and the hydrophobic PS interconnects and BPOSS cages. Interestingly, in the self-assembled Lam structure of BPOSS-PS$_{12}$-DPOSS, the BPOSS cages further form certain crystalline packing within the lamellar confinement, as revealed by the characteristic diffraction peaks of crystalline BPOSS cages in the WAXD pattern. Crystallization of BPOSS cages is prompted by the flat interfaces in the Lam phase. In other three phases with curved interfaces (DG, Hex, and BCC), BPOSS cages are found to be miscible with the PS chains to form the matrix with no ordered packing observed. The phase diagram of the BPOSS-PS$_n$-DPOSS system is experimentally estimated. Shifted phase boundaries compared with symmetric diblock copolymers are observed, which are in good agreement with the reported DPOSS-PS$_n$ system. This effect highlights the unique features of our molecular design to use molecular nanoparticles (such as POSS and functionalized C_{60}) in the development of novel hybrid giant surfactants. Study on these asymmetric giant "bolaform-like" surfactants would provide insights to design and develop novel self-assembling materials at sub-10 nm scales, which are technologically relevant. Further study on this topic is ongoing in our group and will be further discussed in future publications.

ASSOCIATED CONTENT

Supporting Information

Addition characterization data. This material is available free of charge via the Internet at http://pubs.acs.org.

AUTHOR INFORMATION

Corresponding Authors

*E-mail: ky13@zips.uakron.edu (K.Y.).
*E-mail: wenbin@pku.edu.cn (W.-B.Z.).
*E-mail: scheng@uakron.edu (S.Z.D.C.).

Author Contributions

K.W. and M.H. contributed equally to this work.

Funding

This work was supported by NSF (DMR-0906898 and DMR-1408872) and the Joint-Hope Foundation.

Notes

The authors declare no competing financial interest.

ACKNOWLEDGMENTS

The authors thank Kai Guo and Prof. Chrys Wesdemiotis for assistance with MALDI-TOF experiments.

REFERENCES

(1) Whitesides, G. M.; Grzybowski, B. *Science* **2002**, *295*, 2418−2421.
(2) Whitesides, G. M.; Boncheva, M. *Proc. Natl. Acad. Sci. U. S. A.* **2002**, *99*, 4769−4774.
(3) Hawker, C. J.; Russell, T. P. *MRS Bull.* **2005**, *30*, 952−966.
(4) Bates, C. M.; Maher, M. J.; Janes, D. W.; Ellison, C. J.; Willson, C. G. *Macromolecules* **2013**, *47*, 2−12.
(5) Zhang, L.; Eisenberg, A. *Science* **1995**, *268*, 1728−1731.
(6) Bates, F. S. *Science* **1991**, *251*, 898−905.
(7) Bates, F. S.; Fredrickson, G. H. *Annu. Rev. Phys. Chem.* **1990**, *41*, 525−557.
(8) Leibler, L. *Macromolecules* **1980**, *13*, 1602−1617.
(9) Matsen, M. W.; Bates, F. S. *Macromolecules* **1996**, *29*, 1091−1098.
(10) Almdal, K.; Koppi, K. A.; Bates, F. S.; Mortensen, K. *Macromolecules* **1992**, *25*, 1743−1751.
(11) Schulz, M. F.; Bates, F. S.; Almdal, K.; Mortensen, K. *Phys. Rev. Lett.* **1994**, *73*, 86−89.
(12) Zhu, L.; Huang, P.; Cheng, S. Z. D.; Ge, Q.; Quirk, R. P.; Thomas, E. L.; Lotz, B.; Wittmann, J.-C.; Hsiao, B. S.; Yeh, F.; Liu, L. *Phys. Rev. Lett.* **2001**, *86*, 6030−6033.
(13) Park, M.; Harrison, C.; Chaikin, P. M.; Register, R. A.; Adamson, D. H. *Science* **1997**, *276*, 1401−1404.
(14) Jung, Y. S.; Ross, C. A. *Nano Lett.* **2007**, *7*, 2046−2050.
(15) Jung, Y. S.; Chang, J. B.; Verploegen, E.; Berggren, K. K.; Ross, C. A. *Nano Lett.* **2010**, *10*, 1000−1005.
(16) Rodwogin, M. D.; Spanjers, C. S.; Leighton, C.; Hillmyer, M. A. *ACS Nano* **2010**, *4*, 725−732.
(17) Eloi, J.-C.; Rider, D. A.; Wang, J.-Y.; Russell, T. P.; Manners, I. *Macromolecules* **2008**, *41*, 9474−9479.
(18) Ahmed, R.; Patra, S. K.; Chabanne, L.; Faul, C. F. J.; Manners, I. *Macromolecules* **2011**, *44*, 9324−9334.
(19) Hirai, T.; Leolukman, M.; Liu, C. C.; Han, E.; Kim, Y. J.; Ishida, Y.; Hayakawa, T.; Kakimoto, M.; Nealey, P. F.; Gopalan, P. *Adv. Mater.* **2009**, *21*, 4334−4338.
(20) Park, S.; Lee, D. H.; Xu, J.; Kim, B.; Hong, S. W.; Jeong, U.; Xu, T.; Russell, T. P. *Science* **2009**, *323*, 1030−1033.
(21) Cushen, J. D.; Otsuka, I.; Bates, C. M.; Halila, S.; Fort, S.; Rochas, C.; Easley, J. A.; Rausch, E. L.; Thio, A.; Borsali, R.; Willson, C. G.; Ellison, C. J. *ACS Nano* **2012**, *6*, 3424−3433.
(22) Otsuka, I.; Isono, T.; Rochas, C.; Halila, S.; Fort, S.; Satoh, T.; Kakuchi, T.; Borsali, R. *ACS Macro Lett.* **2012**, *1*, 1379−1382.
(23) Isono, T.; Otsuka, I.; Kondo, Y.; Halila, S.; Fort, S.; Rochas, C.; Satoh, T.; Borsali, R.; Kakuchi, T. *Macromolecules* **2013**, *46*, 1461−1469.
(24) Kroto, H. W.; Heath, J. R.; Obrien, S. C.; Curl, R. F.; Smalley, R. E. *Nature* **1985**, *318*, 162−163.
(25) Hirsch, A.; Vostrowsky, O. *Eur. J. Org. Chem.* **2001**, 829−848.
(26) Yu, X.; Zhang, W.-B.; Yue, K.; Li, X.; Liu, H.; Xin, Y.; Wang, C.-L.; Wesdemiotis, C.; Cheng, S. Z. D. *J. Am. Chem. Soc.* **2012**, *134*, 7780−7787.
(27) Lin, Z.; Lu, P.; Hsu, C.-H.; Yue, K.; Dong, X.-H.; Liu, H.; Guo, K.; Wesdemiotis, C.; Zhang, W.-B.; Yu, X.; Cheng, S. Z. D. *Chem.—Eur. J.* **2014**, DOI: 10.1002/chem.201402697.
(28) Baney, R. H.; Itoh, M.; Sakakibara, A.; Suzuki, T. *Chem. Rev.* **1995**, *95*, 1409−1430.
(29) Loy, D. A.; Shea, K. J. *Chem. Rev.* **1995**, *95*, 1431−1442.
(30) Laine, R. M. *J. Mater. Chem.* **2005**, *15*, 3725−3744.
(31) Cordes, D.; Lickiss, P.; Rataboul, F. *Chem. Rev.* **2010**, *110*, 2081−2173.
(32) Kuo, S.-W.; Chang, F.-C. *Prog. Polym. Sci.* **2011**, *36*, 1649−1696.
(33) Kannan, R. Y.; Salacinski, H. J.; Butler, P. E.; Seifalian, A. M. *Acc. Chem. Res.* **2005**, *38*, 879−884.
(34) Cardoen, G.; Coughlin, E. B. *Macromolecules* **2004**, *37*, 5123−5126.
(35) Zhang, W.; Fang, B.; Walther, A.; Müller, A. H. E. *Macromolecules* **2009**, *42*, 2563−2569.
(36) Lee, K. M.; Knight, P. T.; Chung, T.; Mather, P. T. *Macromolecules* **2008**, *41*, 4730−4738.

(37) Hirai, T.; Leolukman, M.; Jin, S.; Goseki, R.; Ishida, Y.; Kakimoto, M.-a.; Hayakawa, T.; Ree, M.; Gopalan, P. *Macromolecules* **2009**, *42*, 8835−8843.
(38) Ahn, B.; Hirai, T.; Jin, S.; Rho, Y.; Kim, K.-W.; Kakimoto, M.-a.; Gopalan, P.; Hayakawa, T.; Ree, M. *Macromolecules* **2010**, *43*, 10568−10581.
(39) Tada, Y.; Yoshida, H.; Ishida, Y.; Hirai, T.; Bosworth, J. K.; Dobisz, E.; Ruiz, R.; Takenaka, M.; Hayakawa, T.; Hasegawa, H. *Macromolecules* **2011**, *45*, 292−304.
(40) Yu, X.; Zhong, S.; Li, X.; Tu, Y.; Yang, S.; Van Horn, R. M.; Ni, C.; Pochan, D. J.; Quirk, R. P.; Wesdemiotis, C.; Zhang, W.-B.; Cheng, S. Z. D. *J. Am. Chem. Soc.* **2010**, *132*, 16741−16744.
(41) Yu, X.; Yue, K.; Hsieh, I.-F.; Li, Y.; Dong, X.-H.; Liu, C.; Xin, Y.; Wang, H.-F.; Shi, A.-C.; Newkome, G. R.; Ho, R.-M.; Chen, E.-Q.; Zhang, W.-B.; Cheng, S. Z. D. *Proc. Natl. Acad. Sci. U. S. A.* **2013**, *110*, 10078−10083.
(42) Zhang, W.-B.; Yu, X.; Wang, C.-L.; Sun, H.-J.; Hsieh, I. F.; Li, Y.; Dong, X.-H.; Yue, K.; Van Horn, R.; Cheng, S. Z. D. *Macromolecules* **2014**, *47*, 1221−1239.
(43) He, J.; Yue, K.; Liu, Y.; Yu, X.; Ni, P.; Cavicchi, K. A.; Quirk, R. P.; Chen, E.-Q.; Cheng, S. Z. D.; Zhang, W.-B. *Polym. Chem.* **2012**, *3*, 2112−2120.
(44) Yue, K.; He, J.; Liu, C.; Huang, M.; Dong, X.-H.; Guo, K.; Ni, P.; Wesdemiotis, C.; Quirk, R.; Cheng, S. D.; Zhang, W.-B. *Chin. J. Polym. Sci.* **2013**, *31*, 71−82.
(45) Yue, K.; Liu, C.; Guo, K.; Wu, K.; Dong, X.-H.; Liu, H.; Huang, M.; Wesdemiotis, C.; Cheng, S. Z. D.; Zhang, W.-B. *Polym. Chem.* **2013**, *4*, 1056−1067.
(46) Wang, Z.; Li, Y.; Dong, X.-H.; Yu, X.; Guo, K.; Su, H.; Yue, K.; Wesdemiotis, C.; Cheng, S. Z. D.; Zhang, W.-B. *Chem. Sci.* **2013**, *4*, 1345−1352.
(47) Su, H.; Li, Y.; Yue, K.; Wang, Z.; Lu, P.; Feng, X.; Dong, X.-H.; Zhang, S.; Cheng, S. Z. D.; Zhang, W.-B. *Polym. Chem.* **2014**, *5*, 3697−3706.
(48) Lin, Z.; Lu, P.; Yu, X.; Zhang, W.-B.; Huang, M.; Wu, K.; Guo, K.; Wesdemiotis, C.; Zhu, X.; Zhang, Z.; Yue, K.; Cheng, S. Z. D. *Macromolecules* **2014**, DOI: 10.1021/ma500696h.
(49) Ash, I.; Ash, M. *Encyclopedia of Surfactants*; Chemical Pub. Co.: New York, 1980.
(50) Yue, K.; Liu, C.; Guo, K.; Yu, X.; Huang, M.; Li, Y.; Wesdemiotis, C.; Cheng, S. Z. D.; Zhang, W.-B. *Macromolecules* **2012**, *45*, 8126−8134.
(51) Zhang, W.-B.; Tu, Y.; Ranjan, R.; Van Horn, R.; Leng, S.; Wang, J.; Polce, M. J.; Wesdemiotis, C.; Quirk, R. P.; Newkome, G. R.; Cheng, S. Z. D. *Macromolecules* **2008**, *41*, 515−517.
(52) Gunes, K.; Isayev, A. I.; Li, X. P.; Wesdemiotis, C. *Polymer* **2010**, *51*, 1071−1081.
(53) Li, Y.; Zhang, W.-B.; Hsieh, I.-F.; Zhang, G.; Cao, Y.; Li, X.; Wesdemiotis, C.; Lotz, B.; Xiong, H.; Cheng, S. Z. D. *J. Am. Chem. Soc.* **2011**, *133*, 10712−10715.
(54) Ma, L.; Geng, H.; Song, J.; Li, J.; Chen, G.; Li, Q. *J. Phys. Chem. B* **2011**, *115*, 10586−10591.
(55) Kolb, H. C.; Finn, M. G.; Sharpless, K. B. *Angew. Chem., Int. Ed.* **2001**, *40*, 2004−2021.
(56) Iha, R. K.; Wooley, K. L.; Nystrom, A. M.; Burke, D. J.; Kade, M. J.; Hawker, C. J. *Chem. Rev.* **2009**, *109*, 5620−5686.
(57) Zhang, W.-B.; He, J.; Yue, K.; Liu, C.; Ni, P.; Quirk, R. P.; Cheng, S. Z. D. *Macromolecules* **2012**, *45*, 8571−8579.
(58) Cheng, L.; Zhang, G. Z.; Zhu, L.; Chen, D. Y.; Jiang, M. *Angew. Chem., Int. Ed.* **2008**, *47*, 10171−10174.
(59) Nonaka, H.; Ouchi, M.; Kamigaito, M.; Sawamoto, M. *Macromolecules* **2001**, *34*, 2083−2088.
(60) Gao, H.; Matyjaszewski, K. *Macromolecules* **2006**, *39*, 4960−4965.
(61) Xi, W.; Scott, T. F.; Kloxin, C. J.; Bowman, C. N. *Adv. Funct. Mater.* **2014**, DOI: 10.1002/adfm.201302847.
(62) Hoyle, C. E.; Bowman, C. N. *Angew. Chem., Int. Ed.* **2010**, *49*, 1540−1573.
(63) Hoyle, C. E.; Lowe, A. B.; Bowman, C. N. *Chem. Soc. Rev.* **2010**, *39*, 1355−1387.
(64) Kade, M. J.; Burke, D. J.; Hawker, C. J. *J. Polym. Sci., Part A: Polym. Chem.* **2010**, *48*, 743−750.
(65) Fox, T. G.; Flory, P. J. *J. Appl. Phys.* **1950**, *21*, 581−591.
(66) Dong, X.-H.; Van Horn, R.; Chen, Z.; Ni, B.; Yu, X.; Wurm, A.; Schick, C.; Lotz, B.; Zhang, W.-B.; Cheng, S. Z. D. *J. Phys. Chem. Lett.* **2013**, *4*, 2356−2360.
(67) Vukovic, I.; Voortman, T. P.; Merino, D. H.; Portale, G.; Hiekkataipale, P.; Ruokolainen, J.; ten Brinke, G.; Loos, K. *Macromolecules* **2012**, *45*, 3503−3512.
(68) Zhu, L.; Cheng, S. Z. D.; Calhoun, B. H.; Ge, Q.; Quirk, R. P.; Thomas, E. L.; Hsiao, B. S.; Yeh, F.; Lotz, B. *J. Am. Chem. Soc.* **2000**, *122*, 5957−5967.
(69) Percec, V.; Cho, W.-D.; Ungar, G. *J. Am. Chem. Soc.* **2000**, *122*, 10273−10281.
(70) Balagurusamy, V. S. K.; Ungar, G.; Percec, V.; Johansson, G. *J. Am. Chem. Soc.* **1997**, *119*, 1539−1555.
(71) Thomas, C. S.; Olsen, B. D. *Soft Matter* **2014**, *10*, 3093−3102.
(72) Dong, X.-H.; Lu, X.; Ni, B.; Chen, Z.; Yue, K.; Li, Y.; Rong, L.; Koga, T.; Hsiao, B. S.; Newkome, G. R.; Shi, A.-C.; Zhang, W.-B.; Cheng, S. Z. D. *Soft Matter* **2014**, *10*, 3200−3208.